ACS APPLIED NANO MATERIALS

www.acsanm.org Article

# Transition-Metal Nanoparticle Catalysts Anchored on Carbon Supports via Short-Chain Alginate Linkers

Joakim Tafjord, Erling Rytter, Anders Holmen, Rune Myrstad, Ingeborg-Helene Svenum, Bjørn E. Christensen, and Jia Yang*

Cite This: *ACS Appl. Nano Mater.* 2021, 4, 3900−3910 Read Online

ACCESS | Metrics & More | Article Recommendations | Supporting Information

**ABSTRACT:** This study reports a green, inexpensive, and highly versatile procedure to synthesize well-dispersed transition-metal nanoparticles anchored on carbon supports. The resulting metal loadings are 26 wt % or above. Achieving both these properties simultaneously has been difficult with established synthesis methods of carbon-supported metal catalysts, such as impregnation and deposition-precipitation. Herein, low-molar-mass sodium alginate with high guluronate content was ion-exchanged with transition-metal ions, followed by a pyrolysis step at 500 °C. The investigated transition-metal ions were $Fe^{3+}$, $Co^{2+}$, $Ni^{2+}$, and $Cu^{2+}$. The alginate's properties and interaction with the transition-metal ions greatly influenced the pyrolyzed material's characteristics, whereas the observed metal particle size was found to negatively correlate with the metal's melting point. The pyrolyzed Fe-alginate was tested as a catalyst for the Fischer−Tropsch synthesis and exhibited an iron time yield of 885 $\mu mol_{CO}\ h^{-1}\ g^{-1}$, which is among the highest activities reported in the literature. The activity is mainly attributed to the iron nanoparticle size achieved by the reported synthesis procedure, and the improved olefin selectivity is ascribed to the sodium and sulfur that originates from the alginate and iron precursor, respectively.

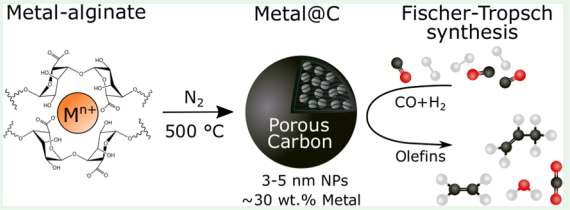


**KEYWORDS:** *alginate, pyrolysis, nanoparticles, carbon support, catalysis, Fischer−Tropsch*

## 1. INTRODUCTION

Nanoscale materials possess high surface-to-volume ratios and quantum size effects, resulting in chemical and physical properties that differ remarkably from their bulk counterparts.[1] In heterogeneous catalysis, reactions often take place at the surface of metal-based materials. Reducing the particle size increases the specific surface area of the catalytically active phase, which frequently improves the activity and reduces the consumption of expensive metals, but may also change the site-specific catalytic rate dramatically.[2−4] Stabilization of catalytic nanoparticles is essential for stable and active performance at elevated temperatures, generally solved by utilizing porous support materials.[5] Loading nanoparticles into a support material is conventionally achieved by introducing a metal precursor solution into the pores of the support by methods such as incipient wetness impregnation or ion exchange, followed by thermal heat treatment.[6] With impregnation, there is often a trade-off between high loadings and small nanoparticles, and while catalyst preparation by use of microemulsions can grant control over the size and morphology of the nanoparticles, preventing agglomeration requires low metal loadings.[7]

Recently, metal−organic frameworks (MOFs) were used as templates to obtain high loading of transition-metal nanoparticles on carbon supports, performed by pyrolysis of the MOFs resulting in the decomposition of organic linkers and crystallization of metal centers.[8] Employing iron-containing MOFs, $Fe_3O_4$ nanoparticles of roughly 3 nm were produced.[9] However, MOFs can be expensive, and instead, we aimed to utilize a cheap and abundant carbon template, namely, alginate.

Alginate is a family of polysaccharides generally produced and extracted from brown algae. They are unbranched biopolymers containing two monomers: (1-4)-linked $\beta$-D-mannuronate (M) and $\alpha$-L-guluronate (G). The G-residues are introduced enzymatically by C-5 epimerases, making the alginate source important for contents and distributions of G-residues. The relative content of G, as well as their diad and triad frequencies, can be determined by nuclear magnetic resonance, which also provides the average length of G-blocks. The GG-diad has traditionally been proposed to adopt a so-called "eggbox" structure (Figure 1a) in the presence of divalent cations such as $Ca^{2+}$.[10] Ca-alginate has been studied extensively for use as biofilms and wound dressing, in addition to enzyme, protein-drug, and bacteria delivery.[11−13] Alginate can also be ion-exchanged with transition-metal ions, although studies on their interaction are scarcer. A density functional

**Received:** January 29, 2021
**Accepted:** March 26, 2021
**Published:** April 7, 2021

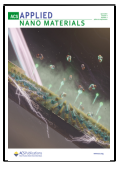

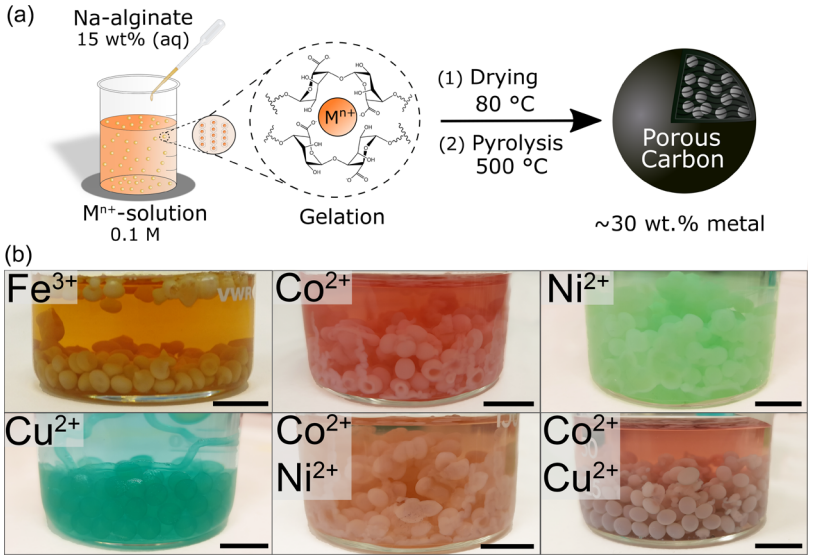


**Figure 1.** (a) Scheme of the general synthesis procedure in this work, involving gelation and pyrolysis. The gelation step illustrates the eggbox structure of alginate guluronate dimers. (b) Na-alginate beads during ion exchange in the respective metal nitrate solutions as indicated in the top left corner. The black scale bars correspond to 1 cm.

theory (DFT)-study suggests that the resulting bonds are more covalent than for $Ca^{2+}$ and alginate.[14]

Dispersing transition-metal ions between alginate chains should provide an excellent foundation for the formation of metal nanoparticles, as cations are atomically dispersed prior to pyrolysis. In previous studies, however, the metal particle size from the pyrolysis of metal-alginates is either not reported or to be 10−30 nm, depending on the transition metal.[15,16] Typically, the employed alginate solutions are 5 wt % or below, possibly limited by the alginate solubility.

Herein, alginate with low molar mass (33 400 Da) and high G content (67%) was utilized, deliberately selected to improve the control of the final metal nanoparticle size. Alginate with lower molar mass allows for higher concentrations of alginate in the solution, while retaining the physical stability of the alginate gel beads. A series of transition metals were studied to investigate metal systems with monometallic Fe, Co, Ni, and Cu and bimetallic CoCu and CoNi. When introducing the metal ions into the alginate matrix, it is important to consider the affinity of specific metal ions to the alginate structure, previously investigated for several divalent cations:[17−19]

$$Pb^{2+} > Cu^{2+} > Cd^{2+} > Ba^{2+} > Sr^{2+} > Ca^{2+} > Co^{2+} > Ni^{2+} > Mn^{2+}$$

A mixture of cations can be introduced simultaneously, but if the goal is to achieve a somewhat similar uptake, the binding strength of the cations must be considered. The binding strength of $Cu^{2+}$ is, for instance, much greater than that of $Co^{2+}$, and consequently, the molar ratio of the $Cu^{2+}Co^{2+}$ system must be tuned to obtain close to equimolar uptake in the alginate gel.

To demonstrate the catalytic performance of a material created by pyrolyzing metal-alginates, one iron catalyst was tested in high-temperature Fischer−Tropsch synthesis (FTS; 340 °C and 20 bar). In FTS, syngas ($CO + H_2$) reacts to form hydrocarbons of varying chain length, while oxygen is removed as $H_2O$. With Fe-catalysts, $H_2O$ and CO may react to form $H_2$ and $CO_2$ through the water-gas shift (WGS) reaction. Due to the additional $H_2$ provided by WGS, syngas from hydrogen-lean feedstocks such as biomass may be used directly.

## 2. EXPERIMENTAL SECTION

**2.1. Materials.** Sodium alginate (LFR 5/60: $F_G \approx 0.65-0.70$, $F_{GG}$, 0.5−0.6, $N_{G>1} \approx 11-20$) was supplied by Dupont Nutrition Norge AS. Iron(III) nitrate nonahydrate (>98%), cobalt(II)nitrate hexahydrate (>98%), nickel(II) nitrate hexahydrate (>98.5%), copper(II) nitrate hemi(pentahydrate) (>98%), potassium bromide (>99%), hydrochloric acid (37%), and nitric acid (70%) were supplied from Sigma-Aldrich. Ethanol (96%) was supplied by VWR. Deionized water was produced by using a Milli-Q water purification system.

**2.2. Synthesis.** Na-alginate was dissolved in deionized water by a magnetic stirrer. 0.15 kg $kg^{-1}$ alginate/water solutions were produced for all samples, in addition to 0.05, 0.10, and 0.20 kg $kg^{-1}$ alginate/water solutions for the iron-containing samples. Metal nitrates solutions were prepared by dissolving the respective salts in deionized water. Solutions of 0.1 M were used for the Fe-, Co-, Ni-, and Cu-alginate samples, and mixture of 0.05 M $Co^{2+}$ and 0.05 M $Ni^{2+}$ for CoNi-alginate. For CoCu-alginate, a mixture of 0.067 and 0.033 M was used for $Co^{2+}$ and $Cu^{2+}$, respectively, due to difference in binding strength. The alginate solutions were added dropwise to their respective metal nitrate solutions, which formed beads on contact (Figure 1). The volume ratio of metal nitrate to alginate solution was always 5:1. The beads were kept in solution for 24 h, then filtered and washed with deionized water three times. The beads were immersed in ethanol−water solutions of increasing concentration over time to gradually transform the beads from hydrogels to alcogels. The initial ethanol concentration was 10% and was increased by 20% every 10th minute up to 90%, by discarding and making a new ethanol−water solution between concentration changes. The beads were ultimately left in a 96% ethanol solution for 24 h. The beads were then collected from the ethanol solution and dried at 80 °C overnight, followed by mortaring.

For pyrolysis, approximately 1 g of the dried powder was placed in a vertical calcination reactor (50 mm i.d.), allowing gas to pass through the sample, which aided the removal of any liquid products that are formed during alginate decomposition. During pyrolysis, 100 mL $min^{-1}$ $N_2$ flowed through the reactor while heating at a rate of 2 °C $min^{-1}$ up to 500 °C, dwelling at 500 °C for 8 h, followed by cooling to room temperature (RT). The samples were then passivated at RT in 50 mL $min^{-1}$ 1% $O_2$ in Ar for 2 h. Passivation was especially important due to the samples' pyrophoric nature, and enables control


https://doi.org/10.1021/acsanm.1c00294
ACS Appl. Nano Mater. 2021, 4, 3900−3910

over the inevitable oxidation process that would take place when contacted with air.

**2.3. Characterization.** Thermogravimetric analysis (TGA) with differential scanning calorimetry (DSC) was performed with a Netzch Jupiter 449 unit. The analyses were performed in an inert atmosphere to study pyrolysis (100 mL $min^{-1}$ in Ar), or an oxidizing atmosphere (75 mL $min^{-1}$ synthetic air + 25 mL $min^{-1}$ Ar). The samples were heated from RT to 900 °C at a heating rate of 10 °C $min^{-1}$. The effluent gases were analyzed with a QMS 403C Aëolos quadrupole mass spectrometer (MS).

The crystalline phases were investigated with powder X-ray diffraction (XRD) at ambient temperature with a Bruker D8 A25 DaVinci X-ray Diffractometer, using a Cu K$\alpha$-radiation ($\lambda$ = 0.15432 nm) X-ray tube and LynxEye SuperSpeed detector. The samples were scanned in the range 2$\Theta$ = 10−80° for 60 min, utilizing a 0.2-degree divergence slit. The powder diffraction files (PDF) used as standards for phase identification were $Fe^0$ (PDF 04-007-9753), $\gamma$-$Fe_3O_4$ (PDF 04-009-2285), $\gamma$-$Fe_2O_3$ (PDF 04-021-3968), $Co^0$ (PDF 04-001-2681), $Co(OH)_2$ (PDF 04-019-0234), $Ni^0$ (PDF 04-010-6148), $Cu^0$ (PDF 04-009-2090) and $Cu_2O$ (PDF 04-007-9767).

$N_2$ adsorption and desorption experiments were performed on a Tristar II 3000. Samples (100 mg) were degassed at 1 mTorr, and 80 °C for 24 h, whereas the pyrolyzed samples employed a temperature of 200 °C. The Brunauer−Emmet−Teller (BET) isotherm and the Barrett−Joyner−Halenda (BJH) method were used to determine specific surface area, pore volume, and pore size distribution.

The elemental loadings were measured by inductively coupled plasma mass spectrometry (ICP-MS). 10−30 mg of dried samples were mixed with 2 mL concentrated nitric acid ($HNO_3$), placed in perfluoroalkoxy alkane (PFA) vials. To aid decomposition the samples were then digested in an UltraClave, where the samples were heated to 245 °C, at a pressure of 50 bar. The resulting solution was diluted to a total volume of 216.6 mL. 16 mL of this solution was sent for analysis along with 3 blank samples that were subtracted from the result. The elemental analysis was performed using a high-resolution inductively coupled plasma ELEMENT 2 connected to a mass spectrometer.

Diffuse reflectance infrared Fourier transform spectroscopy experiments were conducted with a Bruker Tensor II in a Harrick Praying Mantis high-temperature in situ cell, flushed with Ar. Measurements of the background (KBr) and the samples employed a spectral range of 4000−600 $cm^{-1}$, a resolution of 4 $cm^{-1}$, and averaged each sample over 32 scans. The alginic acid reference was synthesized by precipitating 0.05 kg $kg^{-1}$ Na-alginate/water solutions in a HCl solution. The resulting beads were washed in deionized water several times and submerged in ethanol (96%) for 5 min, followed by drying.

The metal oxides and carbon D- and G-bands were analyzed with Raman spectroscopy. Experiments were performed with a Horiba ASD with a laser wavelength of 633 nm, employing a 600 g $mm^{-1}$ grating, ×50 LWD objective, 15 acquisition, 3 accumulations, 10 or 25% filter, and hole of 200. The powdered samples were placed on glass slides for analysis.

The metal particles were imaged using high-resolution transmission electron microscopy (HR-TEM). Experiments were performed with a JEOL JEM-2100 ($LaB_6$-filament, side-mounted Gatan 2k Orius CCD) and a JEOL JEM-2100F (200k Schottky field emission gun (0.7 eV energy spread) and bottom-mounted Gatan 2k Ultrascan CCD) both with Oxford X-Max 80 SDD energy-dispersive X-ray (EDX) (solid angle 0.24 sr) and scanning option with bright-field (BF) and high-angle annular dark-field (HAADF) detector. Samples were suspended in isopropanol, then deposited on a Cu-grid with lacey carbon, or Au-grid in the case of Cu-containing samples, followed by air-drying before imaging.

For X-ray photoelectron spectroscopy (XPS) experiments, the sample powder was pressed onto carbon tape and placed in an Axis UltraDLD XP spectrometer from Kratos. The carbon tape showed no discernible influence on the C 1s spectra. The base pressure in the analysis chamber was between $2 \times 10^{-9}$ and $5 \times 10^{-9}$ Torr during acquisition. Monochromatic Al-K$\alpha$ radiation (1486.6 eV) was used, and the survey spectra and individual core levels were obtained using pass energies of 80 and 20 eV, respectively. Charge compensation was used, and the energy scale was calibrated to $sp^2$-type carbon in the C 1s component at a binding energy of 284.3 eV. A Shirley background was used for all peaks, and the spectra were fitted based on line shapes previously determined by Biesinger et al.,[20,21] where a slight shift in binding energy and/or intensity of the satellite peaks relative to the peak at the lowest binding energy were allowed for some of the oxides and hydroxides.

**2.4. Catalytic Testing.** The Fischer−Tropsch synthesis, experiment was performed in a 10 mm i.d. tubular stainless steel fixed-bed reactor at 340 °C, 20 bar, and $H_2/CO$ = 1.0. The sieved catalyst (0.15 mg, 50−90 $\mu$m) was diluted and mixed with inert SiC (7.0 g, 50−90 $\mu$m) to minimize temperature gradients, and then loaded into the reactor between two plugs of quartz wool to keep the catalyst bed fixed. The reactor was mounted in an electrical furnace, with two aluminum blocks placed around the reactor to further improve heat distribution.[22] The catalyst was reduced in $H_2$ (150 mL $min^{-1}$) at 3 bar with a heating rate of 2 °C $min^{-1}$ to 400 °C, with a dwell time of 3 h. Then, the reactor was cooled to 333 °C and pressurized to 20 bar with 100 000 mL $g^{-1}$ $h^{-1}$ He. Syngas (48.5% CO, 48.5% $H_2$, 3% $N_2$) was then introduced in steps, replacing 20% of the He flow when the temperature had stabilized (5 min), before finally leaving 7% He in the stream. The temperature controller regulated the temperature by reading the furnace temperature, not the bed temperature, due to the inherent delay between furnace heating and how long it takes to effectively heat the catalyst bed temperature. In addition, the exothermic nature of the reaction would amplify the heating effect. An illustration of the furnace and reactor setup is shown in the Supporting Information (Figure S1). The catalyst bed temperature was 337 °C following syngas introduction, which initially decreased rapidly, then stabilized over time. The furnace temperature remained unchanged for the first 78 h on stream, but was then adjusted to reach a bed temperature of 340 °C to gain activity and selectivity data under this condition (Figure S20). The product stream was passed through a hot trap (90 °C) and a cold trap (ambient temperature) to collect liquid Fischer−Tropsch products, such as wax, light hydrocarbons, water, and oxygenates. The remaining gas-phase products were analyzed on an Agilent Technologies 6890N gas chromatograph (GC) equipped with a stainless steel Carbosieve S-II and an HP-plot $Al_2O_3$ column with a thermal conductivity detector (TCD) and flame-ionization detector (FID). The internal GC standard was the 3 vol %. $N_2$ contained in the syngas mixture.

## 3. RESULTS AND DISCUSSION

The characterization of the dried metal-alginates samples is presented and discussed. Acronyms for the dried samples are "Metal(s)"/"Alginate mass %"Alg, e.g., Fe/15Alg, followed by characterization of the pyrolyzed samples, named "Metal(s)"/"initial alginate mass %"C. Second, the performance of an iron sample (Fe/15C) is evaluated for high-temperature FTS.

**3.1. Characteristics of the Dried Samples.** Nitrate salts of $Fe^{3+}$, $Co^{2+}$, $Ni^{2+}$, and $Cu^{2+}$ were employed in the preparation of the aqueous metal solutions as they are highly soluble and have stable oxidation states. The $NO_3^-$ anions should be removed by the washing procedure, and if not, it will decompose to $NO_2$ and $O_2$ during pyrolysis. The resulting metal content (Table 1) was measured by ICP-MS, ranging from 8.8 to 11 wt %. Some of the variations can be explained by the difference in molar mass and the residual Na in the sample.

Due to the trivalent state of $Fe^{3+}$, more charge stabilization is required than for the divalent cations, which might involve three carboxylates from three individual monomers for a single $Fe^{3+}$. If such coordination was present in the Fe/Alg samples it did not lower the metal uptake considerably. All samples were prepared in parallel with the same washing procedure, yet a relatively large difference in Na content was observed. For the



https://doi.org/10.1021/acsanm.1c00294
ACS Appl. Nano Mater. 2021, 4, 3900−3910

**Table 1. Specific Surface Area (BET) and Elemental Loading (ICP-MS) of Elements above 0.01 wt % for the Dried Metal-Alginate Samples**

| sample | surface area ($m^2\ g^{-1}$) | metal 1[a] (wt %) | metal 2[b] (wt %) | Na (wt %) | S (wt %) | Si (wt %) |
|---|---|---|---|---|---|---|
| Fe/5Alg | 218 | 11.7 | | 0.01 | 0.11 | 0.01 |
| Fe/10Alg | 154 | 10.1 | | 0.04 | 0.10 | 0.01 |
| Fe/15Alg | 193 | 9.3 | | 0.05 | 0.07 | 0.01 |
| Fe/20Alg | 178 | 8.8 | | 0.09 | 0.10 | 0.01 |
| Co/15Alg | 15 | 9.2 | | 0.54 | 0.01 | 0.01 |
| Ni/15Alg | 37 | 9.4 | | 0.46 | 0.01 | 0.01 |
| Cu/15Alg | 18 | 11.0 | | 0.14 | 0.02 | 0.01 |
| CoNi/15Alg | 20 | 4.6 | 4.8 | 0.51 | 0.01 | 0.01 |
| CoCu/15Alg | 43 | 3.7 | 5.2 | 0.34 | 0.01 | 0.00 |

[a]wt % of first metal given in sample name. [b]wt % of second metal given in sample name.

divalent cations, Cu/15Alg consistently showed the lowest Na content at a given alginate concentration, having the highest affinity for alginate among the divalent cations. $Fe^{3+}$ was not included in the previously listed binding strength series but is a much stronger Lewis acid than the divalent cations in this work, and will therefore bind more strongly to alginate.[23]

Some sulfur was also present in all samples, but to a larger extent for the Fe-containing samples. This appears to originate from the $Fe(NO_3)_3$ precursor, and not the Na-alginate as the S content in the other samples are much lower. The purity of the metal nitrate salt employed in this work only has >98% purity, in which some impurities may be present. This can be circumvented by employing high-purity precursors. The introduction of small amounts of Na and S through iron precursors has previously been reported by use of ammonium iron citrate.[24] The authors further reported a more thorough study on the effect of Na/S on FTS, which showed an increased $C_2-C_4$ olefin selectivity and decreased methane selectivity, while also improving catalytic activity for supported catalysts.[25]

Different alginate concentrations were employed for the Fe samples, yielding alginate solutions of varying viscosities, in which the limit of dissolvable alginate was the 20 wt % alginate solution. As the metal content decreases and the sodium content increases with increasing alginate concentration, the denseness of the resulting beads appeared to affect diffusion and the extent of successful ion exchange between the iron and sodium ions. For some catalytic systems, alkali like sodium can have adverse effects, but can to a large extent be circumvented by preparing alkali-free and water-soluble alginate precursors, such as ammonium alginate.

The metal cations interact mainly with carboxylates in the alginate. This can be evaluated by investigating the stretching modes of carboxylates with infrared spectroscopy. The bands of interest for metal carboxylates are the relatively strong asymmetric $COO^-$ stretching vibration ($\nu CO_{asym}$) and the weaker symmetric stretching ($\nu CO_{sym}$). The bands' position relative to a free carboxylate ion may indicate which binding modes are present: the uncoordinated carboxylate (i) found in ionic forms such as Na-alginate; for unidentate coordination, (ii) the metal ion is bound to only one of the carboxylate oxygens; in the bidentate chelating coordination, (iii) the cation binds to both carboxylate oxygens; in bidentate bridging coordination, (iv) two distinct cations are bound to one oxygen each in the same carboxylate (Figure 2a). A method for determining binding modes was reported by K. Nakamoto,[26]

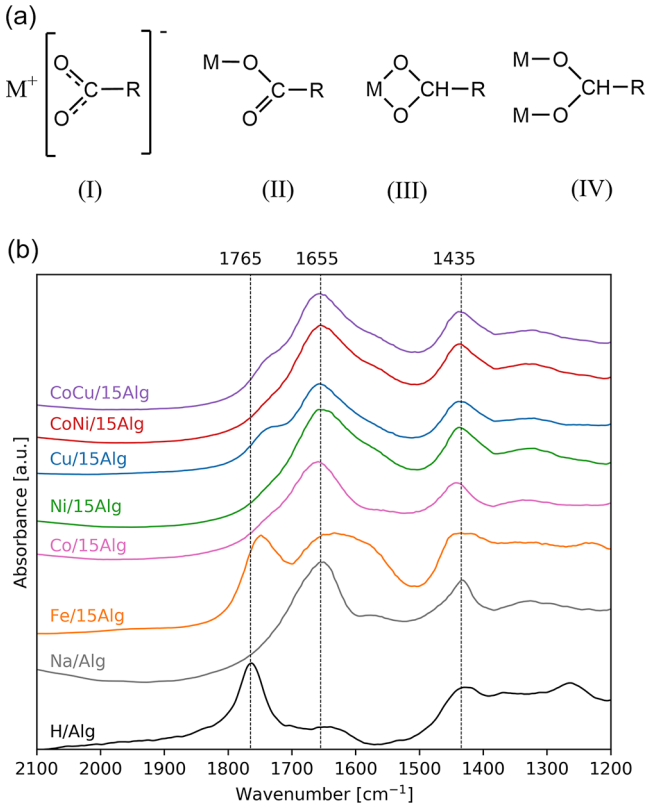


**Figure 2.** (a) Possible interactions between cation (M) and carboxylates. (b) Diffuse reflectance infrared Fourier transform spectra of the dried metal-alginate powder samples, in the spectral range where carboxylic bands are found. Alginic acid (H/Alg) and sodium alginate (Na/Alg) were used as references.

which used the difference ($\Delta\nu$) in wavenumber for $\nu(CO_{sym})$ and $\nu(CO_{asym})$. The binding modes of metal-alginates were determined by comparing their $\Delta\nu$ values with Na-alginate: if the metal-alginate complex obtains a similar $\Delta\nu$ value to Na-alginate, it implies a bridging bidentate mode (iv); a higher value may indicate unidentate coordination (ii); a lower value implies a bidentate chelating mode (iii). All samples with divalent metals yielded a $\Delta\nu$ of roughly 219 $cm^{-1}$, the same as Na/Alg, while Fe/15Alg had a broad $\nu(CO_{asym})$ band around 1635 $cm^{-1}$ and an additional band at 1745 $cm^{-1}$ (Figure 2b). The broad bands of Fe/15Alg indicate a varied chemical environment for the carboxylates. When selecting the peak position of $\nu(CO_{asym})$ at the highest intensity, the resulting $\Delta\nu$ was lower (199 $cm^{-1}$), which implies a shift toward bidentate chelating mode (iii). The additional band (1745 $cm^{-1}$) observed for Fe/15Alg was also found in all of the Fe/Alg samples (Figure S2). As Fe loading decreases, charge compensation in the alginate must be achieved by other means, such as a proton to form alginic acid (−COOH, 1765 $cm^{-1}$), or increased $Fe^{3+}$ coordination with negatively charged functional groups. The 1745 $cm^{-1}$ band has also been observed As(III), for which it was speculated that the band originated from different carboxylate coordination.[27] The low pH (2.0) observed in the $Fe(NO_3)_3$ solution might also have led to the esterification of alginate, meaning a carboxyl and a hydroxyl group from two different monomers form an ester. There was


https://doi.org/10.1021/acsanm.1c00294
ACS Appl. Nano Mater. 2021, 4, 3900−3910

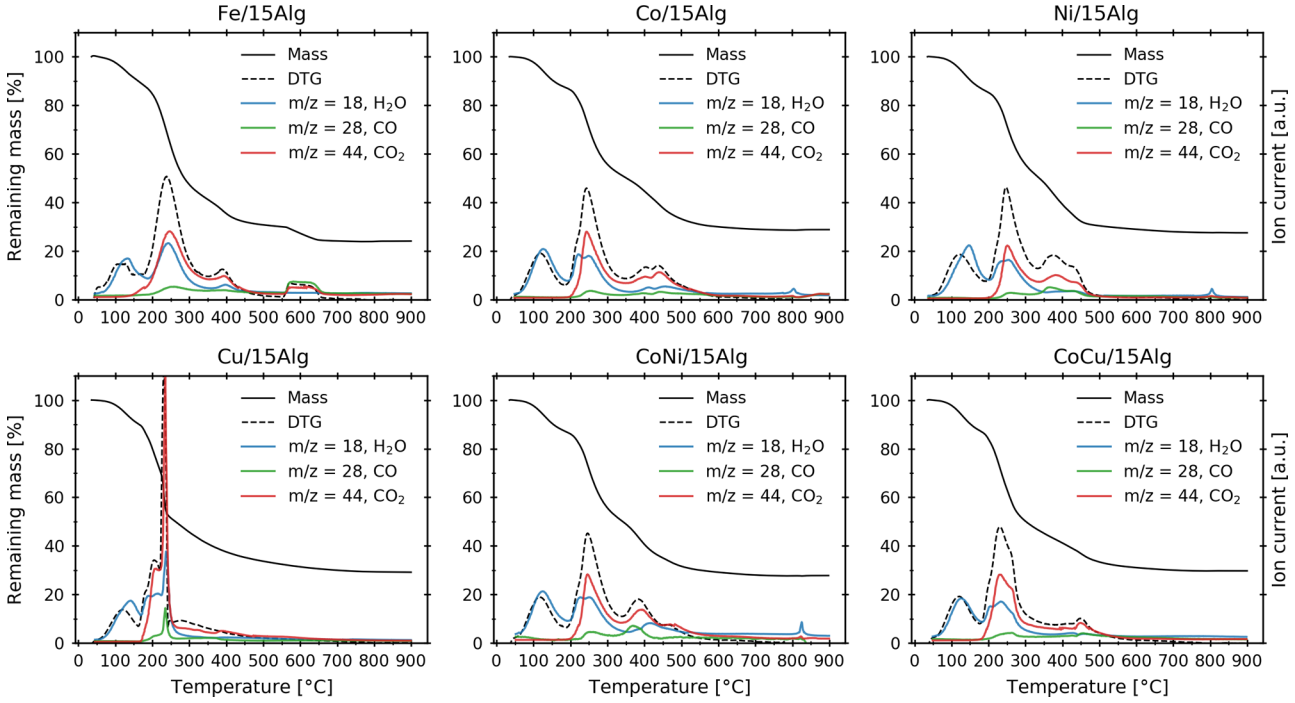


**Figure 3.** Thermogravimetric analysis of the dried samples in Ar from RT to 900 °C at a rate of 10 °C $min^{-1}$. The graphs contain the mass-loss profile and the first derivative of the mass-loss (DTG). The latter is inverted and scaled as a visual aid and for comparison with the effluent gases measured by mass spectrometry.

also a shoulder present around 1720 $cm^{-1}$ for the Cu-containing samples—Cu/15Alg and CoCu/15Alg—that might have originated from a binding mode related to cupric acetate, a distorted octahedral structure of copper alginate.[28,29]

To reduce the surface tension during the ambient drying step, the hydrogel was converted to an alcogel by a solvent exchange with ethanol. The measured $N_2$ adsorption−desorption isotherms after drying did not fit one distinct classification (Figure S3). There was no region where monolayer and multilayer adsorption could be differentiated, which implies a Type II isotherm, in addition to observed features resembling Type IV.[30] The hysteresis loops (H3) of the Fe-alginates did not close and formed a plateau at high relative pressures, indicating that pore condensation did not terminate. The pore system appears to be a mixture of micro-, meso- and macropores. The BET surface area of the dried Fe-alginate samples ranged from 178 to 218 $m^2$ $g^{-1}$ (Table 1), while the other metal-alginates had an order of magnitude lower values, ranging from 15 to 43 $m^2$ $g^{-1}$. Larger surface areas have been reported using supercritical drying, but the employed alginate solutions contained 1−3 wt % alginate.[31] A study using supercritical drying on Cu-alginate with 5, 10, and 15% alginate solutions measured specific surface areas of 111, 25, and 11 $m^2$ $g^{-1}$, respectively.[32] These results imply that alginate concentration had an impact on the surface area in samples with divalent metal ions. In this study, however, the same trend was not observed for the $Fe^{3+}$ samples.

Generally, a negative correlation between porosity and residual Na loading was observed, suggesting that increasing porosity may enhance the effectiveness of washing and sodium removal. We propose that the potential for higher coordination and the alginate affinity of $Fe^{3+}$ had an advantageous effect on porosity, making washing more efficient. This complies with the higher residual Na content observed in the other transition-metal samples with significantly smaller surface areas.

No long-range ordering of metal crystallites was observed with powder X-ray diffraction (XRD, Figure S4). Assuming space-separated coordination sites in the dried samples, no agglomeration of metal particles is expected at this stage.

During pyrolysis, the alginate decomposes to effluent gases, liquids, and solid carbon, a process that was investigated with TGA-MS (Figure 3) and DSC (Figure S5). The initial mass loss can be ascribed to the removal of $H_2O$, by the endothermic process of drying, peaking around 120 °C for all samples. The largest and most rapid material deterioration occurred between 200 and 300 °C, with the removal of carboxylate and possibly hydroxyl functional groups. This was indicated by the increase in effluent $CO_2$ and $H_2O$, processes known as decarboxylation and dehydration, respectively. The decomposition rate of Cu/15Alg was striking, peaking at 231 °C, similar to Na-Alginate (234 °C, Figure S6). Further decomposition occurred between 370 and 450 °C, where $CO_2$ and some $H_2O$ and CO were released. The latter process is known as decarbonylation. During pyrolysis, the metal species will precipitate and possibly undergo transitions between different hydroxides, oxides, and even metallic states. These species are important for stabilizing remaining alginate residues and possibly catalyze different reactions. Decoupling alginate and metal transitions is not straightforward with these techniques as the metal content was roughly 8−11 wt %. Changes in mass due to the metal transitions were relatively small compared to that of alginate decomposition. However, an interesting mass loss step was observed for Fe/15Alg between 550 and 650 °C. This coincided with the release of CO, and some $CO_2$, accompanied by an endothermic DSC signal, indicating reduction to metallic Fe. Temperatures exceeding 600 °C have been reported to reduce metal oxides to metallic particles for other carbonaceous materials, such as


https://doi.org/10.1021/acsanm.1c00294
ACS Appl. Nano Mater. 2021, 4, 3900−3910

polyacrylonitrile, where graphite may act as a reductant.[33] To limit the sintering of metal particles, a reasonable low pyrolysis temperature should be chosen. Furthermore, as the alginate decomposition has mostly concluded at 500 °C, this temperature was chosen for the pyrolysis treatments of metal-alginate samples in this work.

**3.2. Characteristics of the Pyrolyzed Samples.** In preparation for the ICP-MS analysis, difficulties were encountered while decomposing several of the pyrolyzed samples. This was possibly due to the presence of some graphitic carbon. To avoid inconsistency in sample preparation, the elemental loadings were determined by measuring the mass loss in oxidative atmosphere with TGA. By extrapolating the elemental composition from the dried samples (Table 1), the relative amount of sodium, sulfur, and metal was estimated. The metal loading in all samples ranged from 26 to 33 wt % (Table 2). After pyrolysis, an increased BET surface area was

**Table 2. Specific Surface Area (BET, $m^2\ g^{-1}$), Pore Volume ($V_p$, BJH Desorption), and Elemental Loadings (TGA) of Metal-Alginates Pyrolyzed at 500 °C[a]**

| sample | surface area ($m^2\ g^{-1}$) | $V_p$ ($cm^3\ g^{-1}$) | metal 1[b] (wt %) | metal 2[c] (wt %) | Na (wt %) | S (wt %) |
|---|---|---|---|---|---|---|
| Fe/5C | 364 | 0.79 | 26.3 | | 0.02 | 0.24 |
| Fe/10C | 356 | 0.65 | 25.9 | | 0.10 | 0.25 |
| Fe/15C | 357 | 0.71 | 25.8 | | 0.13 | 0.19 |
| Fe/20C | 392 | 0.60 | 26.8 | | 0.27 | 0.30 |
| Co/15C | 214 | 0.07 | 27.0 | | 1.6 | 0.02 |
| Ni/15C | 54 | 0.05 | 33.1 | | 1.6 | 0.03 |
| Cu/15C | 247 | 0.03 | 28.3 | | 0.4 | 0.05 |
| CoNi/15C | 112 | 0.07 | 15.1 | 15.7 | 1.7 | 0.03 |
| CoCu/15C | 196 | 0.11 | 13.5 | 19.0 | 1.2 | 0.03 |

[a]The relative contents of metals, Na, and S are based on the dried samples (Table 1). The trace amounts of Si in the dried samples were not included in this calculation. [b]wt % of first metal given in sample name. [c]wt % of second metal given in sample name

observed for all samples relative to their respective dried samples (Figure S7). The largest relative increase was observed for the samples with small specific surface areas in their dried state (15−43 $m^2\ g^{-1}$). Ni/15C displayed a remarkably smaller surface area (52 $m^2\ g^{-1}$) than the other samples. The bimetallic sample containing Ni, CoNi/15C, had an intermediate surface area (112 $m^2\ g^{-1}$) between Ni/15C and Co/15C (214 $m^2\ g^{-1}$). The Fe samples obtained the largest surface areas after pyrolysis (351−373 $m^2\ g^{-1}$), which were also large in their dried state (154−218 $m^2\ g^{-1}$). These discrepancies suggest that the resulting surface area after pyrolysis is not only dependent on the surface area of the dried sample, but also the metal species and how they affect the decomposition process. The pore sizes and volumes, however, seem to be dependent on the initial porosity, as the Fe/Alg samples obtained relatively large pore volumes (Figure S8). The new-found surface area must be a result of alginate decomposition and the release of effluent gases or liquids that escape the sample. A large surface area in the metal-alginate seemed to aid the formation of pore structures in the mesopore-range during pyrolysis. It is possible, but was not assessed by the methods in this work, that the different metals could catalyze the formation of different volatile and liquid products, whose molecular sizes could impact the resulting pore structure.

The resulting carbon structures after pyrolysis were investigated by Raman spectroscopy (Figure S9). The D-band (1330 $cm^{-1}$) and G-band (1580 $cm^{-1}$) provide information about the bonding mode in carbon materials. The carbonization is often quantified by comparing the intensity ratios ($I_D/I_G$) of these peaks. The highest $I_D/I_G$ was measured for Ni/15C (1.01), whereas Co/15C (0.91) obtained the lowest. Fe/15C (0.93), Cu/15C (0.93), CoNi15/C (0.95), and CoCu/15C (0.95) had intermediate values. Overall, the high D-band intensity suggests that the carbon support was relatively disordered after pyrolysis. XPS was used to analyze the C 1s core-level spectra (Figure S19) in the surface region. Fe/15C had the largest contribution from C═C, while Co/15C and Ni/15C had the lowest. The discrepancy between the XPS and the Raman results might originate from the difference in surface sensitivity and also metal oxide bands that overlap with the D- and G-band, further complicating the assessment of the $I_D/I_G$ ratio. For the Fe/C samples, using 10% laser power resulted in an $I_D/I_G$ ratio of 0.93, as opposed to 1.03 when using 25% power. Ni/15C appeared to contain the least amount of graphitic carbon and showed the largest amount of O−C═O and −C═O contributions in C 1s. This implies that a lower degree of alginate decomposition and graphitization was achieved during pyrolysis.

The metal species were investigated with XRD (Figures 4 and S13), HR-TEM (Figure 5), Raman spectroscopy, and XPS (Figure S18). The TEM images of Fe/15C showed very small spherical Fe particles (3.0 nm) that were densely packed, as expected with a Fe loading of 26 wt %. The Bragg diffractions had low intensities due to amorphous and small crystallite domains. The Fe species appeared to be magnetite ($\gamma$-$Fe_3O_4$) or maghemite ($\gamma$-$Fe_2O_3$), and metallic Fe ($Fe^0$). However, considering the low long-range ordering of the sample, and that maghemite and magnetite have highly similar diffraction patterns, an exact identification was unattainable. The XPS Fe 2p spectrum was fitted to match with 51% $Fe_2O_3$ and 49% ferrihydrite (FeOOH), based on previously determined line profiles.[21] This concurs with the O 1s spectrum that contained both lattice oxygen and hydroxyl groups (see Figure S17). Two-line ferrihydrite is not registered in the International Center of Diffraction data, but generally has two broad peaks at 2Θ around 36° (2.5 Å) and 63° (1.5 Å).[34] These overlap with both magnetite and maghemite, which means that ferrihydrite can neither be excluded nor verified. No evident Raman bands were observed for the Fe/C samples (Figure S10) when using 10% laser power, but increasing the power to 25% led to the appearance of bands that corresponded to hematite ($\alpha$-$Fe_2O_3$). Transformation of iron hydroxides or magnetite to hematite may be induced by the laser. The latter transformation is known as martitization and commonly occurs in nature.[35]

The number-average particle size of Co/15C was slightly larger (5.5 nm) and had a broader size distribution than Fe/15C (Figure S14), but the Bragg diffractions were less defined than for Fe/15C, indicating crystal structures with lower ordering. The diffractions matched with $Co(OH)_2$ and $Co^0$ face-centered cubic (fcc) structure. $Co^0$ is typically stable in hexagonal close packing (hcp) but forms the fcc allotrope at temperatures exceeding 417 °C.[36] The Co 2p spectrum was mainly fitted to $Co(OH)_2$ (65%) and some CoO (35%). The fitted oxygen species in O 1s showed large contributions from −OH (531.5 eV), possibly including oxygen from organic species and lattice defects. The Raman bands corresponded to


https://doi.org/10.1021/acsanm.1c00294
ACS Appl. Nano Mater. 2021, 4, 3900−3910

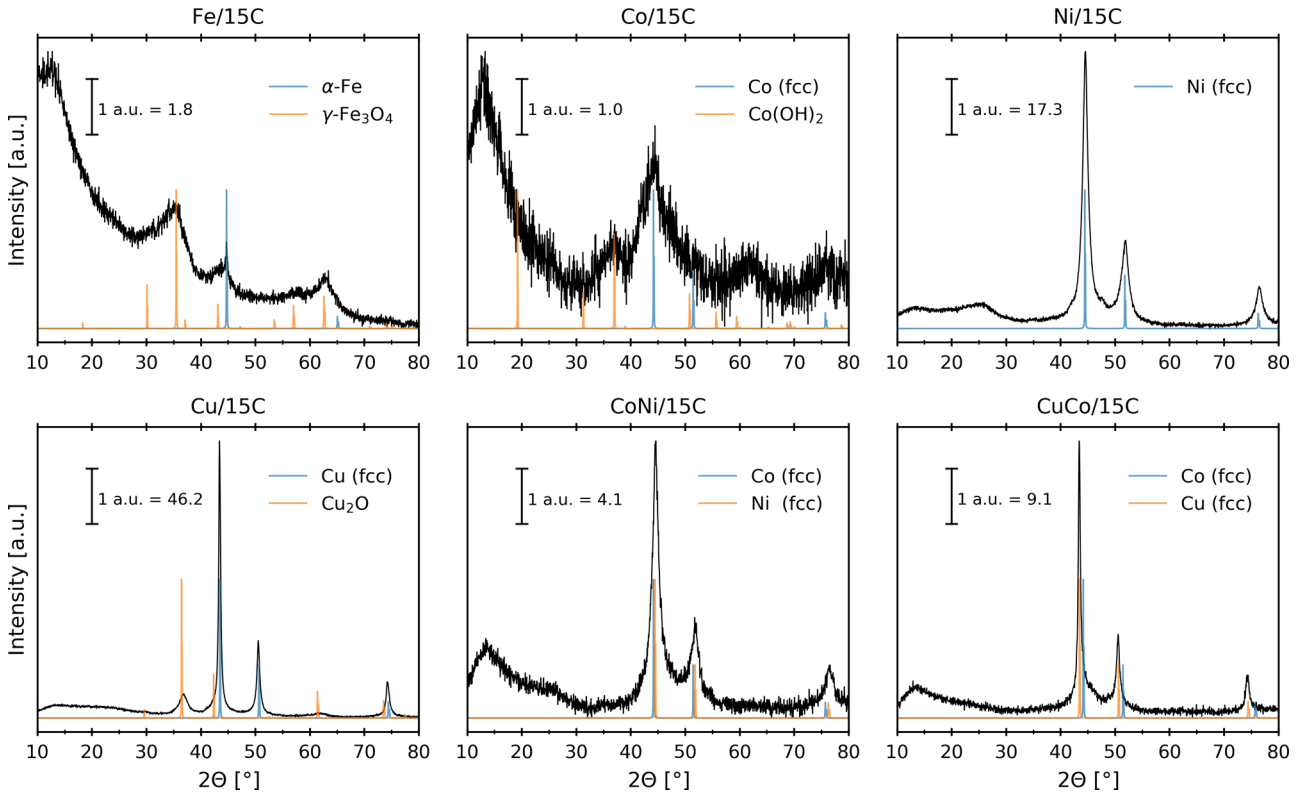


**Figure 4.** X-ray diffractogram (Cu K$\alpha$) of pyrolyzed samples, with a scale bar indicating the intensity difference of the different diffractograms. Standard references are also shown, from powder diffraction files (PDFs) found in Section 2.

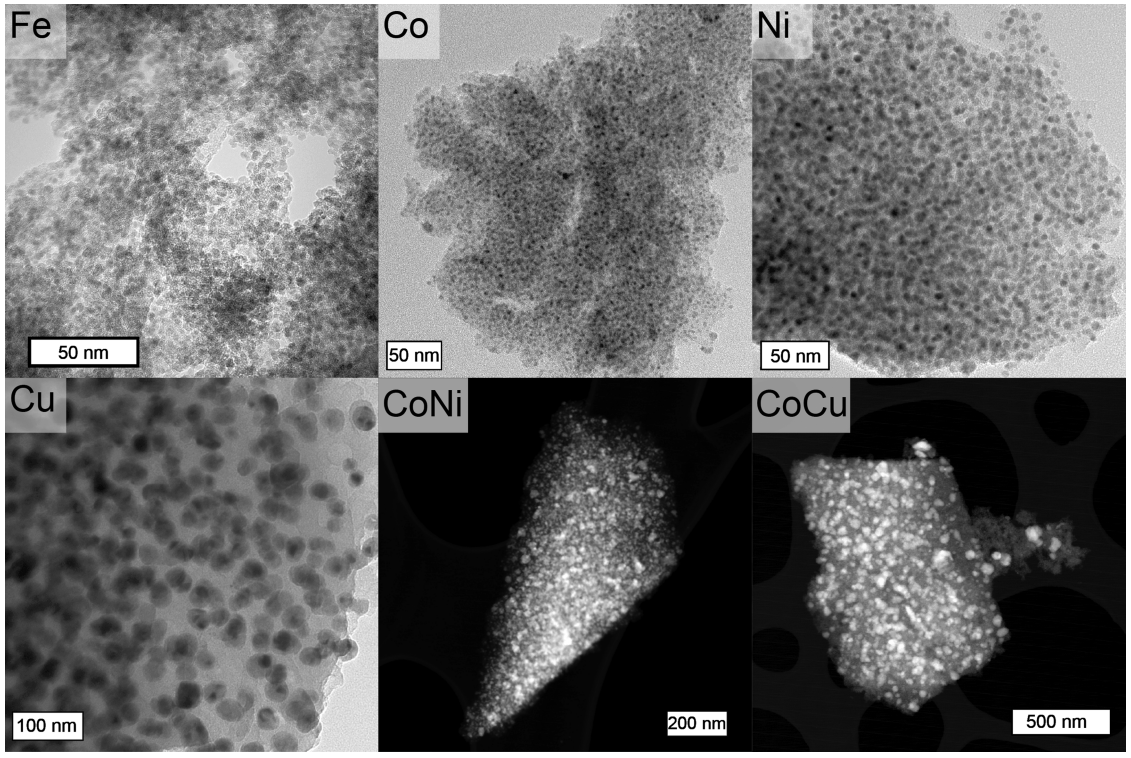


**Figure 5.** TEM bright-field images of Fe/15C, Co/15C, Ni/15C, and Cu/15C, and dark-field images of CoNi/15C and CoCu/15C. A scale bar is located in the lower corner of each image.

$Co_3O_4$, but as with Fe/15C, using 10% laser power did not yield any metal oxide bands. However, $Co_3O_4$ bands appeared when the power was increased to 25% (Figure S11), perhaps as the laser induced a phase transformation from $Co(OH)_2$ to $Co_3O_4$. The hydroxides appear to be surface species.



https://doi.org/10.1021/acsanm.1c00294
ACS Appl. Nano Mater. 2021, 4, 3900−3910

The average particle size of Ni/15C from TEM was 5.1 nm. The Bragg diffractions clearly showed diffractions of $Ni^0$ (fcc), while with Raman, no metal oxides were observed (metallic structures are not Raman-active). The species used to fit the Ni 2p core level of Ni/15C were $Ni^0$ (30%), NiO (20%), $Ni(OH)_2$ (10%), and $\gamma$-NiOOH (40%). The metal oxides and hydroxides can be attributed to less well-ordered oxides or surface species on metallic particles.

Cu/15C sintered to a larger extent than the previously discussed samples, with an average particle size of 22.5 nm. The low melting point of $Cu^0$ makes it more prone to sintering. The Cu species in Cu/15C were mainly $Cu^0$, in addition to some cuprite ($Cu_2O$) that might be surface oxides from the passivation after pyrolysis, or separate oxide particles. No Raman-active bands were observed, but in Cu 2p, the majority of Cu in the surface region was in the form of $Cu(OH)_2$ (65%). The line profiles of $Cu_2O$ and Cu overlap, and a combination of the two constituted the remaining Cu species. Metallic particles of the sizes observed here are expected to have a relatively thick oxide layer, which could dominate the signal in a surface-sensitive technique like XPS.

The average size of metal particles in CoNi/15C was 6.6 nm, some of which were particles in the range of 7−25 nm. The Bragg diffractions corresponded to $Ni^0$ fcc and $Co^0$ fcc, both having very similar lattices, meaning they could potentially form alloys. Energy-dispersive X-ray spectroscopy (EDS, Figure S15) showed some degree of mixing between Co and Ni. The larger particles had a higher density of Ni, while Co particles were smaller and well-dispersed throughout the carbon support. XPS analysis indicated that the metallic fraction of both metals increased relative to their monometallic counterparts. In Co 2p, there was $Co^0$ (50%) in addition to some oxides and hydroxides, while in Ni 2p, the major species was $Ni^0$ (80%). Note that the Ni auger contribution was disregarded. The analysis was based on the pure individual elements, but it is possible to have mixed metal oxides or hydroxides as some mixing of Co and Ni was observed with EDS.

For CoCu/15C, two sets of particles were observed. The first consisted of very small particles in the 3−5 nm range, and the second was larger and more metallic particles in the range of 20−60 nm. EDS analysis (Figure S16) indicated that the larger particles were almost entirely Cu, while the smallest particles were Co. CoCu/15C diffractions matched the $Cu^0$ fcc lattice spacings, although $Co^0$ fcc or an alloy of the two are also possibilities. XPS analysis revealed the presence of $Co^0$ (20%), indicated by EDS to be present in mixed metal particles. The portion of $Cu(OH)_2$ was significantly lower than for Cu/15C, implying that the presence of Co prevents oxidation of $Cu^0$. The Raman bands in both Co/15C and CoCu/15C corresponded to $Co_3O_4$ (Figure S12). The intensities and presence of the $Co_3O_4$ bands in the two samples matched with the amount of $Co(OH)_2$ fitted in their Co 2p spectra, indicating that during the Raman experiments, the laser transformed hydroxides to $Co_3O_4$.

Degree of sintering correlates almost linearly with the melting point of metallic particles.[37] The surface energy of the particles can be altered, by, e.g., promoters, support interaction, and particle shape. Beyond surface energy, the atmosphere and vicinity to other particles (e.g., metal loading) are important sintering factors. The melting points for metallic Fe, Co, Ni, and Cu are 1538, 1495, 1455, and 1085 °C, respectively, and the observed particle sizes in this work reflect this to an extent. This comparison assumes metallic particles, which is not necessarily the case. Herein, only ex situ measurements of crystalline phases exposed to oxygen were performed, effectively limiting our insight of crystalline phases during pyrolysis. Many of the metal oxides and hydroxides observed during characterization after pyrolysis might have formed after passivation or in contact with air. However, it is reasonable to assume that the samples that were metallic after passivation also were metallic at the later stages of the pyrolysis. Sintering could be reduced by decreasing the pyrolysis temperature. However, our preliminary pyrolysis experiments at 400 °C on Fe-alginate samples yielded a dramatic decrease in surface area and porosity. The temperature was not sufficient to carburize the alginate, similar to that observed for pyrolysis of Fe-MOFs.[38] Thus, to reduce sintering, a possible improvement would be to reduce metal loading for species that are prone to sintering, such as Cu. In future work, the pyrolysis process will be investigated by in situ measurements such as XRD and X-ray absorption spectroscopy to elucidate the fate of the metal species.

**3.3. Fischer−Tropsch Synthesis.** To display this novel synthesis method's ability to produce highly active catalysts, Fe/15C was tested under high-temperature FTS conditions: 340 °C, 20 bar, and a $H_2/CO$ ratio of 1.0. Care was taken during activation, as a rapid introduction of syngas leads to extreme heat development, despite the catalyst being diluted with SiC to 2 wt % of the bed. The heat originates from the exothermic nature of both FTS and WGS.

A high initial CO conversion (Figure 6) was observed, meaning the iron was rapidly transformed to iron carbide in contact with syngas. The decline in activity over time may be attributed to Fe phase changes and sintering, which also led to a decrease in bed temperature over time. The catalyst selectivity is a temperature-dependent property. As such, after 78 h on stream, the temperature was increased to achieve a bed temperature of 340 °C (Figure S20) and to obtain

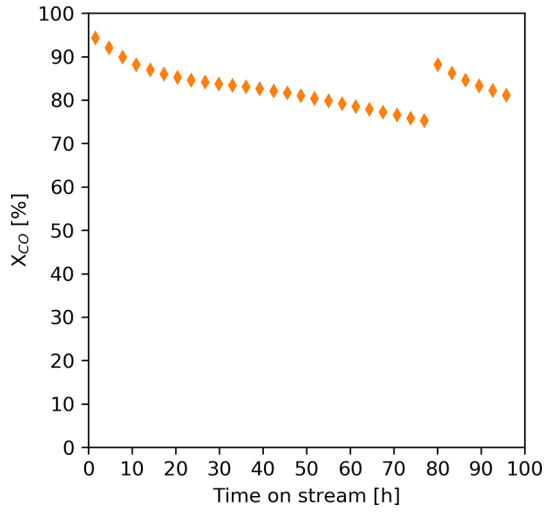


**Figure 6.** After reduction of Fe/15C at 400 °C for 3 h in $H_2$, Fischer−Tropsch synthesis was performed at $P$ = 2 MPa, $H_2/CO$ = 1, $W$ = 150 mg, GHSV = 100 000 mL $g^{-1}$ $h^{-1}$, with an initial temperature of approximately 340 °C. CO conversion as a function of time-on-stream. Due to a decrease in activity and consequently decreased reactor temperature, the bed temperature was adjusted to 340 °C after 78 h on stream.



https://doi.org/10.1021/acsanm.1c00294
ACS Appl. Nano Mater. 2021, 4, 3900−3910

Table 3. Catalytic Activity and Product Selectivity of Fe/15C Compared to Some State-of-the-Art Fe Catalysts for the Fischer−Tropsch synthesis at $T$ = 340 °C, $P$ = 20 bar, and $H_2/CO$ = 1.0[a]

| sample | $X_{CO}$ (%) | TOS (h) | GHSV ($h^{-1}$) | ITY ($\mu mol_{CO}\ g_{Fe}^{-1}\ s^{-1}$) | $CO_2$-free selectivity | | | | |
|---|---|---|---|---|---|---|---|---|---|
| | | | | | $CO_2$ (%) | $CH_4$ (%) | $C_2-C_4o$ (%) | $C_2-C_4p$ (%) | $C_{5+}$ (%) |
| Fe/15C | 83 | 90 | 34 000 | 885 | 46 | 17 | 29 | 15 | 39 |
| Fe@C-500[38] | 76 | 80 | 30 000 | 360 | 46 | 15 | 14 | 29 | 42 |
| Fe-Na-S/$\alpha$-$Al_2O_3$[24] | 79 | 64 | 1500 | 26 | 41 | 17 | 39 | 19 | 14 |
| 9Fe@CNF[40] | 18 | 100 | 54 000 | 400 | 33 | 35 | 36 | 15 | 14 |

[a]A more comprehensive list can be found in the Supporting Information (Table S3).

selectivity data at this temperature. A comparison of the activity and selectivity of Fe/15C with other state-of-the-art iron catalysts from the literature performed under similar conditions is shown in Table 3. After 90 h on stream, Fe/15C exhibited high activity (885 $\mu mol_{CO}\ g_{Fe}^{-1}\ s^{-1}$) in terms of iron time yield (ITY) compared to other recent iron nanocatalysts (Table S3). We propose that the activity to a large extent can be attributed to the nanoparticle size, which yields a large surface area for catalytic activity. In addition, there is a possible added increase in activity from the Na/S promotion originating from the iron precursor, similar to that previously reported for Fe-Na-S/$\alpha$-$Al_2O_3$.[24] The Fe/C samples obtained relatively high porosity with both micro- and mesopores, which was attributed to the binding strength and coordination effect of $Fe^{3+}$ in Fe-alginate. The effect of hierarchical pore systems for iron supported on carbon catalysts for FTS is still a matter that requires further investigation. However, one hypothesis is that micropores assist the dispersion of iron nanoparticles, while meso- and macropores may enhance mass transfer and also tune the FTS product selectivity.[39] In addition, carbon supports have weak metal−support interactions, which is favorable for the reducibility and formation of iron carbides.

The $C_2-C_4$ olefins selectivity ($C_2-C_4o$, 29%) was high, while both methane (17%) and $C_2-C_4$ paraffin ($C_2-C_4p$, 15%) selectivity were relatively low. The Fe@C-500 MOF-derived catalyst[38] showed very similar material characteristics to Fe/15C, but our material exhibited much greater olefin selectivity. We attribute this to the Na/S promotion provided by the $Fe(NO_3)_3$ and Na-alginate precursors, which resulted in enhanced olefin selectivity and suppressed methane production. With the surface carbide mechanism, Na/S has been proposed to promote termination via $\beta$-hydride elimination, which has been shown to be effective on weakly interacting and inert carbon supports.[39]

## 4. CONCLUSIONS

In this work, a novel and generic, yet simple method to prepare highly dispersed transition-metal nanoparticles supported on carbon was developed. The method shows great potential as a means to produce highly active heterogeneous catalysts. The unique feature of the catalyst materials is high metal loading (>26 wt %) combined with small nanoparticles (3−5 nm) with a narrow size distribution. The metal particle size was found to correlate with the melting point of the metals, where lower melting points (e.g., Cu) resulted in larger metallic particles. Moreover, the iron-containing samples exhibited a relatively large BET surface area and mesoporous pore sizes, which is affected by the pores present in the Fe-alginate before pyrolysis. The enhanced porosity of observed for Fe-alginate is attributed to the binding strength and coordination effects of $Fe^{3+}$. Bimetallic samples showed some degree of alloying, which assisted the formation of metal nanoparticles, and appeared to be more prone to sintering than their monometallic counterparts. The iron-based catalyst was tested for FTS as a model reaction. The activity proved exceptionally high (ITY = 885 $\mu mol_{CO}\ g_{Fe}^{-1}\ s^{-1}$), which can largely be attributed to the size of the iron nanoparticles. The catalyst demonstrated favorable selectivity toward lower olefins (29%) owing to the promoter effect of Na and S present in the alginate and iron precursors.

## ■ ASSOCIATED CONTENT

### Supporting Information

The Supporting Information is available free of charge at https://pubs.acs.org/doi/10.1021/acsanm.1c00294.

Metal nitrate salts employed for the different samples and the concentrations of the solutions (Table S1); reactor and oven setup in the Fischer−Tropsch synthesis experiment (Figure S1); DRIFTS of the dried Fe-alginate samples (Figure S2); $N_2$ adsorption−desorption isotherms of dried metal-alginate samples (Figure S3); powder X-ray-diffractograms of the dried metal-alginate samples (Figure S4); TGA and DSC analysis of dried alginate samples (Figure S5); TGA of Na-alginate (Figure S6); $N_2$ adsorption−desorption isotherms of the pyrolyzed samples (Figure S7); pore size distribution (BJH desorption) of the pyrolyzed samples (Figure S8); Raman spectra of D- and G-band for the pyrolyzed samples(Figure S9); Raman spectra of metal oxide bands in Fe/15C, Co/15C and CoCu/15C (Figure S10, S11 and S12); powder X-ray diffractograms of the pyrolyzed samples (Figure S13); particle size distribution of the pyrolyzed samples from TEM (Figure S14); TEM-EDS mapping of CoNi/15C (Figure S15); TEM-EDS line scan of CoCu/15C (Figure S16); XPS survey spectra of the pyrolyzed samples (Figure S17); fitted XPS spectra of metal 2p for the pyrolyzed samples (Figure S18); fitted XPS spectra of C 1s and O 1s for the pyrolyzed samples (Figure S19); and loading (wt %) of carbon, oxygen, sodium, and metals based on XPS results (Table S2); reactor temperature throughout the FTS experiment (Figure S20); $CO_2$ selectivity, and $CO_2$-free hydrocarbon selectivities as a function of time on stream during FTS (Figure S21); and comparison of the activity of recent iron nanocatalysts in FTS (Table S3) (PDF)



https://doi.org/10.1021/acsanm.1c00294
ACS Appl. Nano Mater. 2021, 4, 3900−3910

## AUTHOR INFORMATION


### Corresponding Author

**Jia Yang** − *Department of Chemical Engineering, Norwegian University of Science and Technology, 7491 Trondheim, Norway*; Email: jia.yang@ntnu.no

### Authors

**Joakim Tafjord** − *Department of Chemical Engineering, Norwegian University of Science and Technology, 7491 Trondheim, Norway*; orcid.org/0000-0002-1034-8356

**Erling Rytter** − *Department of Chemical Engineering, Norwegian University of Science and Technology, 7491 Trondheim, Norway*

**Anders Holmen** − *Department of Chemical Engineering, Norwegian University of Science and Technology, 7491 Trondheim, Norway*; orcid.org/0000-0001-7967-9711

**Rune Myrstad** − *Department of Process Technology, SINTEF Industry, 7034 Trondheim, Norway*

**Ingeborg-Helene Svenum** − *Department of Chemical Engineering, Norwegian University of Science and Technology, 7491 Trondheim, Norway; Department of Materials and Nanotechnology, SINTEF Industry, 7034 Trondheim, Norway*

**Bjørn E. Christensen** − *Department of Biotechnology and Food Science, Norwegian University of Science and Technology, 7491 Trondheim, Norway*; orcid.org/0000-0001-9640-0225

Complete contact information is available at: https://pubs.acs.org/10.1021/acsanm.1c00294


### Notes

The authors declare no competing financial interest.

## ACKNOWLEDGMENTS

This study was financially supported by the Department of Chemical Engineering, Norwegian University of Science and Technology, through the Strategic Funding Program.

## REFERENCES


(1) Roduner, E. Size matters: why nanomaterials are different. *Chem. Soc. Rev.* **2006**, *35*, 583−592.

(2) Bezemer, G. L.; Bitter, J. H.; Kuipers, H. P.; Oosterbeek, H.; Holewijn, J. E.; Xu, X.; Kapteijn, F.; van Dillen, A. J.; de Jong, K. P. Cobalt particle size effects in the Fischer-Tropsch reaction studied with carbon nanofiber supported catalysts. *J. Am. Chem. Soc.* **2006**, *128*, 3956−3964.

(3) Carballo, J. M. G.; Yang, J.; Holmen, A.; García-Rodríguez, S.; Rojas, S.; Ojeda, M.; Fierro, J. L. G. Catalytic effects of ruthenium particle size on the Fischer−Tropsch Synthesis. *J. Catal.* **2011**, *284*, 102−108.

(4) den Breejen, J.; Radstake, P.; Bezemer, G.; Bitter, J.; Frøseth, V.; Holmen, A.; de Jong, K. On the origin of the cobalt particle size effects in Fischer-Tropsch catalysis. *J. Am. Chem. Soc.* **2009**, *131*, 7197−7203.

(5) Cao, A.; Lu, R.; Veser, G. Stabilizing metal nanoparticles for heterogeneous catalysis. *Phys. Chem. Chem. Phys.* **2010**, *12*, 13499−13510.

(6) White, R. J.; Luque, R.; Budarin, V. L.; Clark, J. H.; Macquarrie, D. J. Supported metal nanoparticles on porous materials. Methods and applications. *Chem. Soc. Rev.* **2009**, *38*, 481−494.

(7) Eriksson, S. Preparation of catalysts from microemulsions and their applications in heterogeneous catalysis. *Appl. Catal., A* **2004**, *265*, 207−219.

(8) Shen, K.; Chen, X.; Chen, J.; Li, Y. Development of MOF-Derived Carbon-Based Nanomaterials for Efficient. *ACS Catal.* **2016**, *6*, 5887−5903.

(9) Santos, V. P.; Wezendonk, T. A.; Jaen, J. J.; Dugulan, A. I.; Nasalevich, M. A.; Islam, H. U.; Chojecki, A.; Sartipi, S.; Sun, X.; Hakeem, A. A.; Koeken, A. C.; Ruitenbeek, M.; Davidian, T.; Meima, G. R.; Sankar, G.; Kapteijn, F.; Makkee, M.; Gascon, J.; et al. Metal organic framework-mediated synthesis of highly active and stable Fischer-Tropsch catalysts. *Nat. Commun.* **2015**, *6*, No. 6451.

(10) Martinsen, A.; Skjåk-Bræk, G.; Smidsrød, O. Alginate as Immobilization Material: I. Correlation between Chemical and Phyiscal Properties of Alginate Gel Beads. *Biotechnol. Bioeng.* **1989**, *33*, 79−89.

(11) Pawar, S. N.; Edgar, K. J. Alginate derivatization: A review of chemistry, properties and applications. *Biomaterials* **2012**, *33*, 3279−3305.

(12) Omtvedt, L. A.; Dalheim, M. O.; Nielsen, T. T.; Larsen, K. L.; Strand, B. L.; Aachmann, F. L. Efficient Grafting of Cyclodextrin to Alginate and Performance of the Hydrogel for Release of Model Drug. *Sci. Rep.* **2019**, *9*, No. 9325.

(13) Sandvig, I.; Karstensen, K.; Rokstad, A. M.; Aachmann, F. L.; Formo, K.; Sandvig, A.; Skjåk-Bræk, G.; Strand, B. L. RGD-peptide modified alginate by a chemoenzymatic strategy for tissue engineering applications. *J. Biomed. Mater. Res., Part A* **2015**, *103*, 896−906.

(14) Agulhon, P.; Markova, V.; Robitzer, M.; Quignard, F.; Mineva, T. Structure of Alginate Gels: Interaction of Diuronate Units with Divalent Cations from Density Functional Calculations. *Biomacromolecules* **2012**, *13*, 1899−1907.

(15) Latorre-Sanchez, M.; Primo, A.; Garcia, H. Green synthesis of $Fe_3O_4$ nanoparticles embedded in a porous carbon matrix and its use as anode material in Li-ion batteries. *J. Mater. Chem.* **2012**, *22*, 21373−21375.

(16) Brayner, R.; Vaulay, M.-J.; Fiévet, F.; Coradin, T. Alginate-Mediated Growth of Co, Ni, and CoNi Nanoparticles: Influence of the Biopolymer Structure. *Chem. Mater.* **2007**, *19*, 1190−1198.

(17) Haug, A.; Smidsrød, O.; et al. Selectivity of some anionic polymers for divalent metal ions. *Acta Chem. Scand.* **1970**, *24*, 843−854.

(18) Patrón-Prado, M.; Acosta-Vargas, B.; Serviere-Zaragoza, E.; Méndez-Rodríguez, L. C. Copper and Cadmium Biosorption by Dried Seaweed Sargassum sinicola in Saline Wastewater. *Water, Air, Soil Pollut.* **2010**, *210*, 197−202.

(19) Rowbotham, J. S.; Dyer, P. W.; Greenwell, H. C.; Selby, D.; Theodorou, M. K. Copper(II)-mediated thermolysis of alginates: a model kinetic study on the influence of metal ions in the thermochemical processing of macroalgae. *Interface Focus* **2013**, *3*, No. 20120046.

(20) Biesinger, M. C.; Lau, L. W. M.; Gerson, A. R.; Smart, R. S. C. Resolving surface chemical states in XPS analysis of first row transition metals, oxides and hydroxides: Sc, Ti, V, Cu and Zn. *Appl. Surf. Sci.* **2010**, *257*, 887−898.

(21) Biesinger, M. C.; Payne, B. P.; Grosvenor, A. P.; Lau, L. W. M.; Gerson, A. R.; Smart, R. S. C. Resolving surface chemical states in XPS analysis of first row transition metals, oxides and hydroxides: Cr, Mn, Fe, Co and Ni. *Appl. Surf. Sci.* **2011**, *257*, 2717−2730.

(22) Borg, Ø.; Eri, S.; Blekkan, E. A.; Storsæter, S.; Wigum, H.; Rytter, E.; Holmen, A. Fischer−Tropsch synthesis over γ-alumina-supported cobalt catalysts: Effect of support variables. *J. Catal.* **2007**, *248*, 89−100.

(23) Pearson, R. G. Hard and soft acids and bases. *J. Am. Chem. Soc.* **1963**, *85*, 3533−3539.

(24) Torres Galvis, H. M.; Bitter, J. H.; Khare, C.; Ruitenbeek, M.; Dugulan, A. I.; De Jong, K. P. Supported Iron Nanoparticles as Catalysts for Sustainable Production of Lower Olefins. *Science* **2012**, *335*, 835−838.

(25) Torres Galvis, H. M.; Koeken, A. C.; Bitter, J. H.; Davidian, T.; Ruitenbeek, M.; Dugulan, A. I.; de Jong, K. P. Effects of sodium and sulfur on catalytic performance of supported iron catalysts for the

Fischer−Tropsch synthesis of lower olefins. *J. Catal.* **2013**, *303*, 22−30.
(26) Nakamoto, K. *Infrared Spectra of Inorganic and Coordination Compounds*; Wiley: New York, 1997.
(27) Zaafarany, I. Temperature Dependence of Electrical Conductivity for Some Natural Coordination Polymeric Biomaterials Especially Some Cross-Linked Trivalent Metal Alginate Complexes with Correlation between the Coordination Geometry and Complex Stability. *J. Adv. Chem. Eng.* **2014**, *4*, No. 1000111.
(28) van Niekerk, J. N.; Schoening, F. R. L. A new type of copper complex as found in the crystal structure of cupric acetate, Cu2(CH3COO)4.2H2O. *Acta Crystallogr.* **1953**, *6*, 227−232.
(29) Hassan, R. M.; Makhlouf, M. T.; El-Shatoury, S. A. Alginate polyelectrolyte ionotropic gels. Part IX: Diffusion control effects on the relaxation time of sol-gel transformation for transition-divalent metal alginate ionotropic gel complexes. *Colloid Polym. Sci.* **1992**, *270*, 1237−1242.
(30) Sing, K. S. W. Reporting physisorption data for gas/solid systems with special reference to the determination of surface area and porosity (Recommendations 1984). *Pure Appl. Chem.* **1985**, *57*, 603−619.
(31) Horga, R.; di Renzo, F.; Quignard, F. Ionotropic alginate aerogels as precursors of dispersed oxide phases. *Appl. Catal., A* **2007**, *325*, 251−255.
(32) Baldino, L.; Cardea, S.; Scognamiglio, M.; Reverchon, E. A new tool to produce alginate-based aerogels for medical applications, by supercritical gel drying. *J. Supercrit. Fluids* **2019**, *146*, 152−158.
(33) Yang, Z.; Shen, J.; Archer, L. A. An in situ method of creating metal oxide−carbon composites and their application as anode materials for lithium-ion batteries. *J. Mater. Chem.* **2011**, *21*, 11092−11097.
(34) Michel, F. M.; Ehm, L.; Liu, G.; Han, W. Q.; Antao, S. M.; Chupas, P. J.; Lee, P. L.; Knorr, K.; Eulert, H.; Kim, J.; Grey, C. P.; Celestian, A. J.; Gillow, J.; Schoonen, M. A. A.; Strongin, D. R.; Parise, J. B.; et al. Similarities in 2- and 6-Line Ferrihydrite Based on Pair Distribution Function Analysis of X-ray Total Scattering. *Chem. Mater.* **2007**, *19*, 1489−1496.
(35) Mazzetti, L.; Thistlethwaite, P. J. Raman spectra and thermal transformations of ferrihydrite and schwertmannite. *J. Raman Spectrosc.* **2002**, *33*, 104−111.
(36) WARD, L. *Cobalt (Co)*; PALIK, E. D., Ed.; Academic Press: Boston, 1998; pp 435−448.
(37) Nanda, K. K.; Sahu, S. N.; Behera, S. N. Liquid-drop model for the size-dependent melting of low-dimensional systems. *Phys. Rev. A* **2002**, *66*, No. 013208.
(38) Wezendonk, T. A.; Santos, V. P.; Nasalevich, M. A.; Warringa, Q. S.; Dugulan, A. I.; Chojecki, A.; Koeken, A. C.; Ruitenbeek, M.; Meima, G.; Islam, H.-U.; Sankar, G.; Makkee, M.; Kapteijn, F.; Gascon, J. Elucidating the nature of Fe species during pyrolysis of the Fe-BTC MOF into highly active and stable Fischer−Tropsch catalysts. *ACS Catal.* **2016**, *6*, 3236−3247.
(39) Chen, Y.; Wei, J.; Duyar, M. S.; Ordomsky, V. V.; Khodakov, A. Y.; Liu, J. Carbon-based catalysts for Fischer−Tropsch synthesis. *Chem. Soc. Rev.* **2021**, *50*, 2337−2366.
(40) Xie, J.; Torres Galvis, H. M.; Koeken, A. C.; Kirilin, A.; Dugulan, A. I.; Ruitenbeek, M.; de Jong, K. P. Size and Promoter Effects on Stability of Carbon-Nanofiber-Supported Iron-Based Fischer-Tropsch Catalysts. *ACS Catal.* **2016**, *6*, 4017−4024.


https://doi.org/10.1021/acsanm.1c00294
*ACS Appl. Nano Mater.* 2021, 4, 3900−3910